https://doi.org/10.1007/s41230-024-3031-z

Effect of Mn content on microstructure and properties of AlCrCuFeMn$_x$ high-entropy alloy

Ning Wang[1], Kai Ma[1], Qiu-da Li[3], Yu-dong Yuan[1], Yan-chun Zhao[1], and *Li Feng[1, 2]

1. School of Materials Science and Engineering, Lanzhou University of Technology, Lanzhou 730050, China

2. State Key Laboratory of Advanced Processing and Reuse of Nonferrous Metals, Lanzhou 730050, China

3. CNNC Nuclear Power Operation and Management Co., Ltd., Haiyan 314300, Zhejiang, China

Abstract: AlCrCuFeMn$_x$ (x=0, 0.5, 1, 1.5, and 2) high-entropy alloys were prepared using the vacuum arc melting technology. The microstructure and mechanical properties of AlCrCuFeMn$_x$ were analyzed and tested by XRD, SEM, TEM, nanoindentation, and electronic universal testing. The results indicate that the AlCrCuFeMn$_x$ high-entropy alloy exhibits a dendritic structure, consisting of dendrites with a BCC structure, interdendrite regions with an FCC structure, and precipitates with an ordered BCC structure that form within the dendrite. Manganese (Mn) has a strong affinity for dendritic, interdendritic, and precipitate structures, allowing it to easily enter these areas. With an increase in Mn content, the size of the precipitated nanoparticles in the dendritic region initially increases and then decreases. Similarly, the area fraction initially decreases and then increases. Additionally, the alloy's strength and wear resistance decrease, while its plasticity increases. The AlCrCuFeMn$_{1.5}$ alloy boasts excellent mechanical properties, including a hardness of 360 HV and a wear rate of 2.4×10^{-5} mm^3·N^{-1}·mm^{-1}. It also exhibits impressive yield strength, compressive strength, and deformation rates of 960 MPa, 1,700 MPa, and 27.5%, respectively.

Keywords: high-entropy alloys; microstructure; mechanical properties; wear resistance; strengthening mechanisms

CLC numbers: TG146.21 **Document code:** A **Article ID:** 1672-6421(2024)02-147-12

1 Introduction

High-entropy alloys are widely employed in surface engineering due to their thermodynamic high-entropy effect, kinetic hysteresis diffusion, structural lattice distortion, and unique cocktail effect of properties [1-4]. Compared to conventional metallic materials, high-entropy alloys often exhibit superior properties such as higher strength, hardness [5-7], wear resistance [8], corrosion resistance [9-11], and temperature oxidation resistance [12-13]. Adjusting the proportion of elements in high-entropy alloys can alter their crystal structure and microstructure, leading to improved strength and wear resistance. Liu et al. [14] prepared a multi-component Al$_x$CoCrCuFeNi high-entropy alloy (x=0, 0.5, 1, 1.5, and 2) by vacuum arc melting. The results indicated that an increase in the Al element content leads to a refined structure and improved hardness and wear resistance of the alloy. Additionally, the presence of Al elements led to the formation of a passivation layer, which enhanced its corrosion resistance in salt solutions.

The presence of Mn in high-entropy alloys is critical, as it regulates the phase stability of the alloy, alters its deformation mechanism, and can induce either the twinning-induced plasticity (TWIP) or phase transformation-induced plasticity (TRIP) effect. As a result, Mn plays a crucial role in the behavior of duplex high-entropy alloys [15-17]. Furthermore, since Mn is an FCC phase-forming element, increasing its content raises the volume fraction of the FCC phase in high-entropy alloys. This increase has an impact on the compressibility, wear resistance, and corrosion resistance of the alloy. Therefore, Mn is often used as one of the important primary elements when designing the composition of high-entropy alloys. Li et al. [18] prepared Fe$_{80-x}$Mn$_x$Co$_{10}$Cr$_{10}$ high-entropy alloys. They attempted to reduce the phase stability of the alloy by reducing the Mn content to achieve the crystal structure transformation from FCC single-phase to FCC+HCP dual-phase. Moreover, the generation of a

***Li Feng**

Male, born in 1981, Ph.D, Professor. His research interests mainly focus on simulation study of solidification microstructure by phase field method, cold spraying additive manufacturing technology, and high entropy alloy coating. To date, he has published more than 50 papers.

E-mail: fenglils@lut.edu.cn

Authors Ning Wang and Kai Ma contributed equally to this paper.

Received: 2023-03-02; Accepted: 2023-04-10

dual-phase structure in the alloy can result in two significant strengthening mechanisms: interfacial hardening and phase hardening. This breaks the mutual constraints of strength and plasticity that are present in traditional metallic materials, and allows the obtaining of sub-stable high-entropy alloys that exhibit both extremely high strength and plasticity. Wu et al. [19] explored the evolution of Mn on the microscopic morphology and mechanical properties of $CoCrCu_{0.1}Fe_{0.15}Mo_{1.5}Mn_xNi$ (x=0.05, 0.12, and 0.3) alloys. The results showed that the alloy has a dendritic structure, and the volume fraction of the FCC phase increases with an increase in Mn content. When the Mn content was increased from 0.05at.% to 0.3at.%, the hardness of the alloy decreased from 715 HV to 392 HV.

In this study, inexpensive elements such as Fe, Cr, Al, Cu, and Mn were chosen as the primary components. The $AlCrCuFeMn_x$ high-entropy alloys lump with a stable solid solution phase were prepared using vacuum arc melting technology. The impact of varying Mn content on the phase, structure, and mechanical properties of these alloys was systematically studied.

2 Materials and methods

The raw materials used in this experiment were commercial metal monomers particles required for the preparation of alloying materials. The raw materials were proportioned according to the atomic molar ratio of $AlCrCuFeMn_x$ (x=0, 0.5, 1, 1.5, and 2) high-entropy alloys, where the purity of each elemental material was greater than 99.9wt.% and the ingredient weight of each sample was 20 g. Due to the volatility of the Mn element, an additional 0.2 g to 0.3 g of Mn particles per sample was required. The alloy ingots were prepared in a non-self-consuming vacuum arc melting furnace, and each sample was melted five times in order to ensure the homogeneity of the alloy ingot composition. The resulting alloy ingots were cylinders having a diameter of Φ20 mm and a height of 10 mm.

The phase constitution of the polished alloy samples was analyzed using a D/MAX2500PC X-ray diffractometer (XRD) with a scan speed of 4°·min^{-1}, a scan step of 0.02°, an accelerating voltage of 40 kV, a current of 40 mA, and a diffraction angle ranging between 20° and 90°. The QuantaFEG450 field emission scanning electron microscopy (SEM) and energy spectrometry (EDS) were used to analyze the microstructure and microzone composition of the high-entropy alloy. The hardness of the specimen was measured using a HV1,000 micro hardness tester, selected on the Vickers scale. More precisely, 5 points on the surface of the specimen were measured, and the obtained values were then averaged. The room temperature compression test of the alloy was conducted on a WDW-100D electronic universal material testing machine at a speed of 1 mm·min^{-1}. The tested specimen was a cylinder having a diameter of 5 mm and a height of 10 mm. The UMT-Tribolab friction equipment produced by BRUKER Company in the United States was used. In addition, alumina balls having a diameter of Φ6 mm were used as the counter-grinding parts to test the tribological properties of the alloy under dry sliding conditions at room temperature. Each small ball was wiped clean with alcohol, and the friction method was reciprocating. The friction testing parameters were set to a loading load of 5 N, a friction stroke of 3 mm, a frequency of 3 Hz, and a friction time of 20 min.

To determine the influence of the microstructure of the alloy on the local microhardness, nanoindentation tests were performed on the alloy using an Anton Paar type nanoindenter. The employed press needle was a diamond Berkovich needle set to a load control mode of 5 mN. Ten points were pressed on the surface of the specimen and then averaged.

3 Results and discussion

3.1 Phase constitution analysis of $AlCrCuFeMn_x$ high-entropy alloys

Figure 1 shows the X-ray diffraction patterns of $AlCrCuFeMn_x$ high-entropy alloys with different Mn contents. It can be seen that there are two crystal structures in the alloys: the face-centered cubic (FCC) crystal structure and body-centered cubic (BCC) crystal structure. As the Mn content (x) increases from 0 to 2, the diffraction peaks of the $AlCrCuFeMn_x$ high-entropy alloys remain relatively constant, still consisting of FCC+BCC phases. However, an increase in the Mn content leads to a gradual increase in the diffraction peak intensity of FCC phase. This suggests that the addition of Mn is beneficial for the formation of the FCC phase in the alloy.

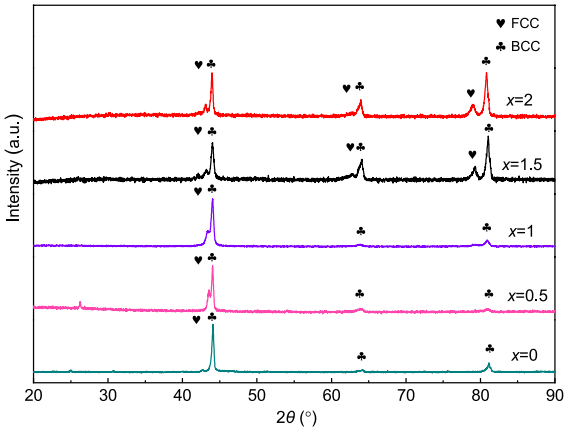

Fig. 1: XRD patterns of $AlCrCuFeMn_x$ high-entropy alloys

Zhang et al. [20] have identified several parameters that play an indicative role in determining the formation of solid solutions in high-entropy alloys, such as mixing enthalpy (ΔH_{mix}), mixing entropy (ΔS_{mix}), valence electron concentration (VEC), and atomic size difference (δ). The thermodynamic parameters of the $AlCrCuFeMn_x$ high-entropy alloy were obtained by calculation [Eqs. (1)–(4)]. The results are shown in Table 1.

$$VEC = \sum_{i=1}^{n} C_i (VEC)_i \quad (1)$$

$$\Delta S_{\text{mix}} = -R\sum_{i=1}^{n} C_i \ln C_i \quad (2)$$

$$\Delta H_{\text{mix}} = 4\sum_{i=1, i\neq j}^{n} \Delta H_{ij}^{\text{mix}} C_i C_j \quad (3)$$

$$\delta = 100\sqrt{\sum_{i=1}^{n} C_i\left(1-\frac{r_i}{\bar{r}}\right)^2} \quad (4)$$

where n is the number of element species in the alloy, C_i is the atomic percentage of the ith component, VEC_i is the valence electron concentration of the ith element, R is the gas constant (R=8.314 J·mol^{-1}·K^{-1}), H_{ij}^{mix} is the mixed enthalpy of binary pairs for the ith and jth elements, and r_i and $\bar{r}$ are the atomic radius and average atomic radius of the ith element.

Based on the calculation results, the AlCrCuFeMn$_x$ high-entropy alloys exhibit δ values of no more than 5.042% and ΔH_{mix} values ranging from −7.916 to −5.000 kJ·mol^{-1}. The stable solid solution structures can easily form in high-entropy alloys when $\delta \leq 6.6\%$ and −15 kJ·mol^{-1}<ΔH_{mix}<5 kJ·mol^{-1} [21], solid solutions containing a mixture of BCC and FCC structures can form when the VEC is between 6.87 and 8.0 [22]. The VEC values of the AlCrCuFeMn$_x$ high-entropy alloys in the present study are all 7. This is because the VEC value of the Mn element is 7. An increase in the Mn content of the AlCrCuFeMn$_x$ high-entropy alloys does not alter its FCC+BCC two-phase solid solution structure or the VEC value.

Table 1: Standard parameters of solid solution of AlCrCuFeMn$_x$ high-entropy alloys

Alloy	VEC	ΔS_{mix} (J·K^{-1}·mol^{-1})	ΔH_{mix} (kJ·mol^{-1})	δ (%)
AlCrCuFe	7	1.386R	−5.000	5.042
AlCrCuFeMn$_{0.5}$	7	1.581R	−6.509	4.775
AlCrCuFeMn$_1$	7	1.610R	−7.360	4.615
AlCrCuFeMn$_{1.5}$	7	1.595R	−7.816	4.990
AlCrCuFeMn$_2$	7	1.562R	−7.916	4.278

3.2 Microstructural and morphological analysis of AlCrCuFeMn$_x$ high-entropy alloys

SEM photographs of AlCrCuFeMn$_x$ high-entropy alloys with different Mn contents in Fig. 2 indicate the influence of Mn content on the microstructure evolution of the alloy. Without addition of Mn, the microstructure of the alloy consists of the light grey interdendrites and dark grey dendrites. The dendritic region (DR) is larger and the interdendritic region (ID) is smaller. As the Mn content increases from x=0 to x=2, the dendritic region decreases while the interdendritic region increases. This is attributed to the rise in FCC structure resulting from the increase in Mn content. Figure 3 shows the EDS maps of AlCrCuFe and AlCrCuFeMn$_1$ high-entropy alloys. Figure 3(a) reveals that Fe and Cr elements are concentrated in the dendritic region, while Cu elements are concentrated in the interdendritic region of the AlCrCuFe alloy. Additionally, Al elements are uniformly distributed throughout the alloy. Compared to the AlCrCuFe alloy, the distribution of Fe, Cr, Cu, and Al elements in different regions of the AlCrCuFeMn$_1$ alloy remains relatively unchanged. Additionally, the Mn element is uniformly distributed throughout the alloy. The EDS maps for AlCrCuFeMn$_x$ (x=0.5, 1.5, 2) high-entropy alloys resemble those in Fig. 3 and will not be reiterated here.

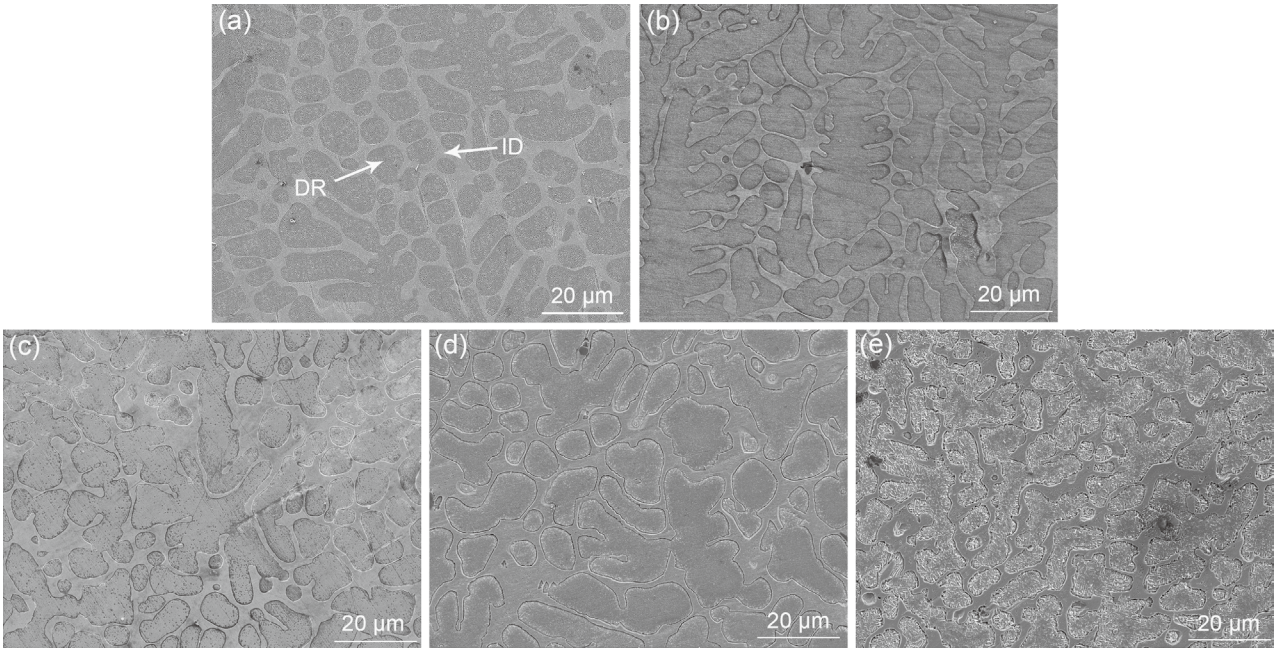

Fig. 2: SEM morphologies of AlCrCuFeMn$_x$ high-entropy alloys: (a) x=0; (b) x=0.5; (c) x=1; (d) x=1.5; (e) x=2

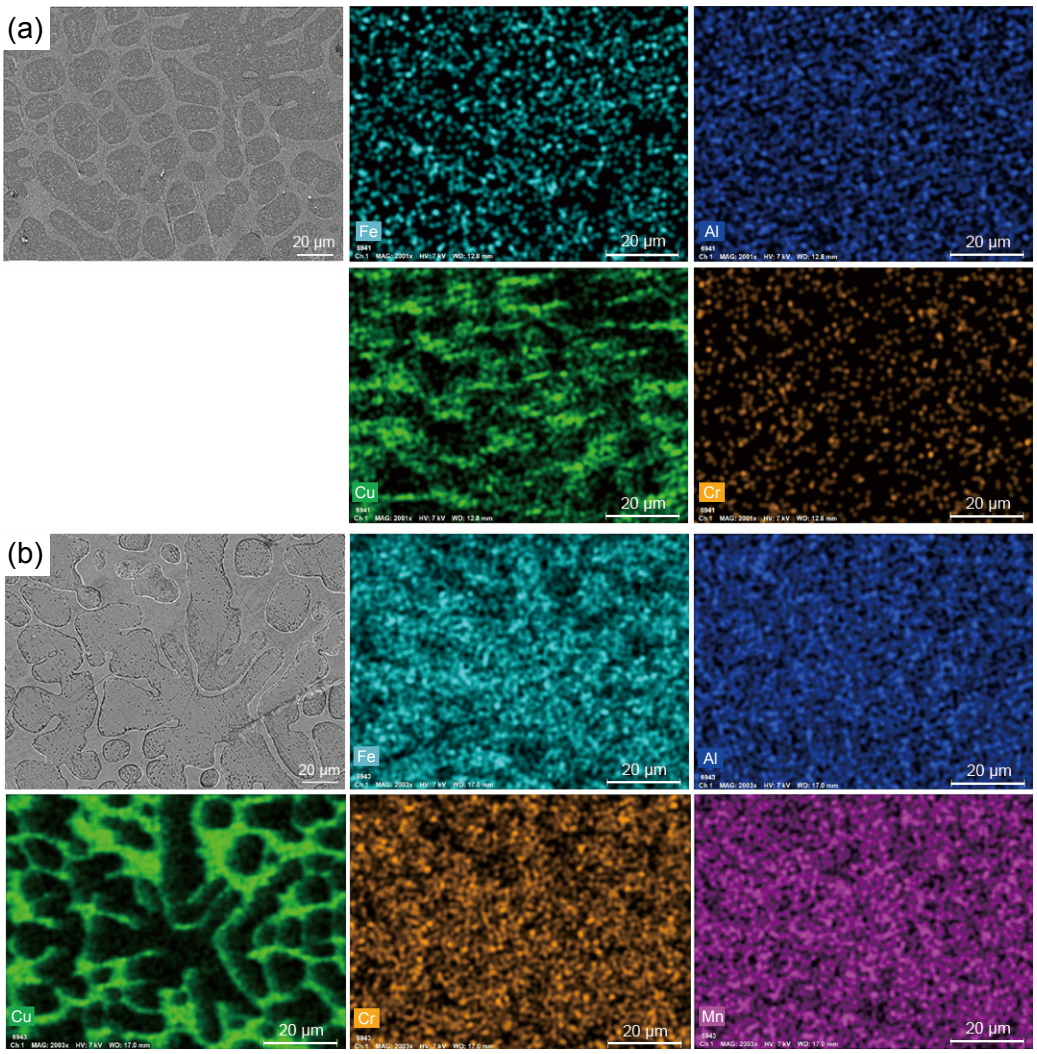

Fig. 3: EDS maps of AlCrCuFe (a) and AlCrCuFeMn$_1$ (b) high-entropy alloys

The area fraction of dendritic and interdendritic regions in the AlCrCuFeMn$_x$ high-entropy alloys were counted using the Image-pro Plus software for multiple fields of view. The results are presented in Table 2. It can be seen that the area fraction of dendritic structure in the high-entropy alloy is the greatest when the Mn content is x=0. With the addition of Mn, the area fraction of dendritic structure in the alloy gradually decreases while that of the interdendritic structure gradually increases. The area fraction of interdendritic structure reaches the maximum of 49.8% at x=2. This indicates that the Mn element promotes the formation of interdendritic structures in the alloy. Due to the fact that the Mn element promotes the formation of FCC structures, as mentioned above, it can be inferred that the interdendritic structures are FCC structures, which will be confirmed in the later tests.

Table 2: Area fraction (%) of dendritic and interdendritic structures of AlCrCuFeMn$_x$ high-entropy alloys with different Mn contents

Alloys	Dendritic structure	Interdendritic structure
AlCrCuFe	72.1	27.9
AlCrCuFeMn$_{0.5}$	68.1	31.9
AlCrCuFeMn$_1$	56.2	43.8
AlCrCuFeMn$_{1.5}$	52.5	47.5
AlCrCuFeMn$_2$	50.2	49.8

To further analyze the microstructure of the AlCrCuFeMn$_x$ alloy, transmission electron microscopy analysis was employed. Figures 4, 5, and 6 display the TEM bright field (BF) images of the AlCrCuFe, AlCrCuFeMn$_1$, and AlCrCuFeMn$_{1.5}$ high-entropy alloys, along with the selected area electron diffraction (SAED) patterns of the various phases. Figure 4(a) shows two distinct phases: light grey and dark grey. By analyzing the energy spectra presented in Figs. 3 and 8, it can be concluded that the light grey region corresponds to the dendritic structure, while the dark grey region corresponds to the interdendritic structure. Long strips with a length of approximately 110 nm uniformly precipitated on the dendrites, and a large number of nanotwins appear between the dendrites. Based on the SAED patterns shown in Figs. 4(b) and (c), it can be concluded that the dendrite structure in the AlCrCuFe high-entropy alloy is a disordered BCC structure, while the interdendrite structure is a disordered FCC structure. Additionally, the long strips of precipitates on the dendrites exhibit ordered BCC structures, as shown in Figs. 4–7.

Figures 5 and 6 demonstrate that the phase constitution of the $AlCrCuFeMn_1$ and $AlCrCuFeMn_{1.5}$ high-entropy alloys remains unchanged, consisting of FCC and BCC phases. This is consistent with that of the AlCrCuFe high-entropy alloy. However, the nanotwins present between the dendrites gradually decrease, and the long precipitates on the dendrites increase from 110 nm at x=0 to nearly 170 nm at x=1, and then decrease to approximately 130 nm at x=1.5.

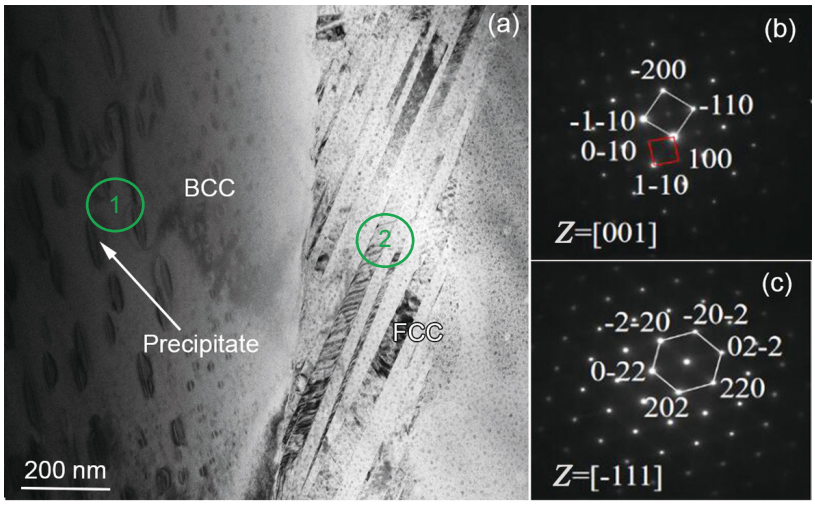

Fig. 4: TEM microstructure and SEAD images of AlCrCuFe high-entropy alloy: (a) bright field TEM image; (b) SAED of the BCC phase along the [001] axis (Region 1); (c) SAED of FCC phase along the [–111] axis (Region 2)

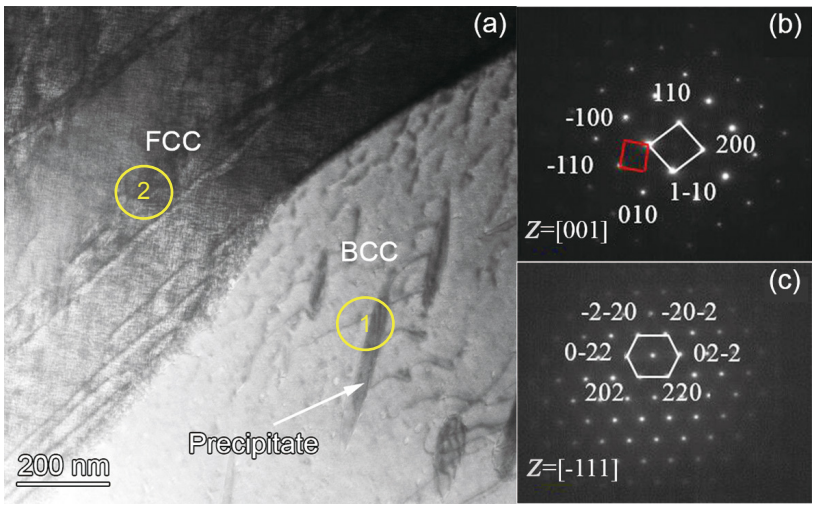

Fig. 5: TEM microstructure and SEAD images of $AlCrCuFeMn_1$ high-entropy alloy: (a) bright field TEM image; (b) SAED of the BCC phase along the [001] axis (Region 1); (c) SAED of FCC phase along the [–111] axis (Region 2)

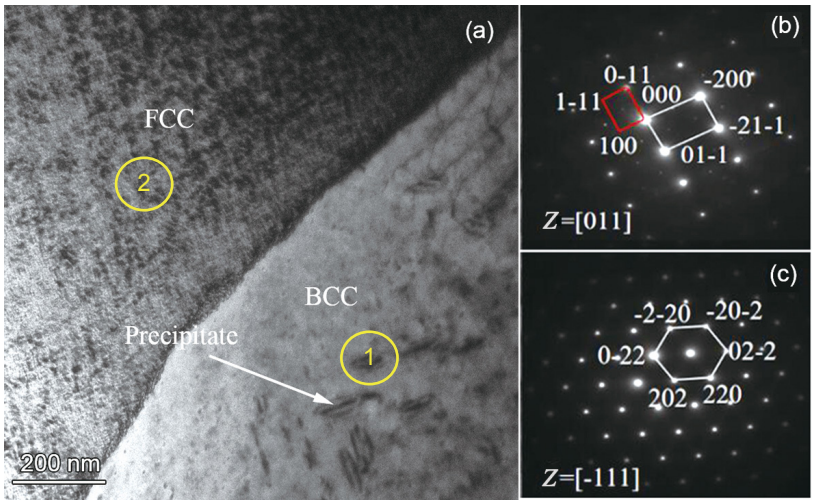

Fig. 6: TEM microstructure and SEAD images of $AlCrCuFeMn_{1.5}$ high-entropy alloy: (a) bright field TEM image; (b) SAED of the BCC phase along the [001] axis (Region 1); (c) SAED of FCC phase along the [–111] axis (Region 2)

Figure 7 shows a high-resolution TEM image taken from the <001> direction and the fast Fourier transform (FFT) pattern of the $AlCrCuFeMn_1$ high-entropy alloy. The FFT pattern further confirms that the dendritic matrix maintains a disordered BCC structure, the precipitated particles have an ordered BCC structure, and a co-lattice relationship is maintained between the precipitates and matrix phase.

To visualize the distribution state of the elements in the alloy, TEM-STEM analysis was performed on the $AlCrCuFeMn_1$ high-entropy alloy. Figure 8 shows the elemental distribution of the $AlCrCuFeMn_1$ alloy in HADDF and STEM mode. It can be seen that in the BCC region, the matrix has a higher content of Fe, Cr, and Mn elements and a relatively lower content of Cu elements. However, the precipitated particles have a relatively higher content of Cu elements and a relatively lower content of Fe and Cr elements. The FCC region is enriched in Cu elements, with relatively lower levels of Fe and Cr elements. The Al element is uniformly distributed throughout the grain, because the mixing enthalpy between Al and the other elements is negative and the interatomic chemical affinity between the elements is good, so no segregation occurs. The elemental composition of each phase in the alloy was initially determined by the above analysis.

To study the influence of Mn addition on the phase transformation of $AlCrCuFeMn_x$, the chemical composition of different phases in the three high-entropy alloys (AlCrCuFe, $AlCrCuFeMn_1$, and $AlCrCuFeMn_{1.5}$) was measured by STEM-EDS. The results are shown in Table 3. In the AlCrCuFe alloy, the BCC phase is the FeCr-rich phase, the FCC phase is the AlCu-rich phase, and the long strips of precipitated phase are the Cu-rich phase. When Mn elements are added, the interdendritic region of the $AlCrCuFeMn_x$ high-entropy alloys changes from an AlCu-rich FCC phase to an AlCuMn-rich FCC phase. The addition of Mn to the high-entropy alloy reduces the content of Cu elements in the FCC phase, thereby eliminating Cu segregation.

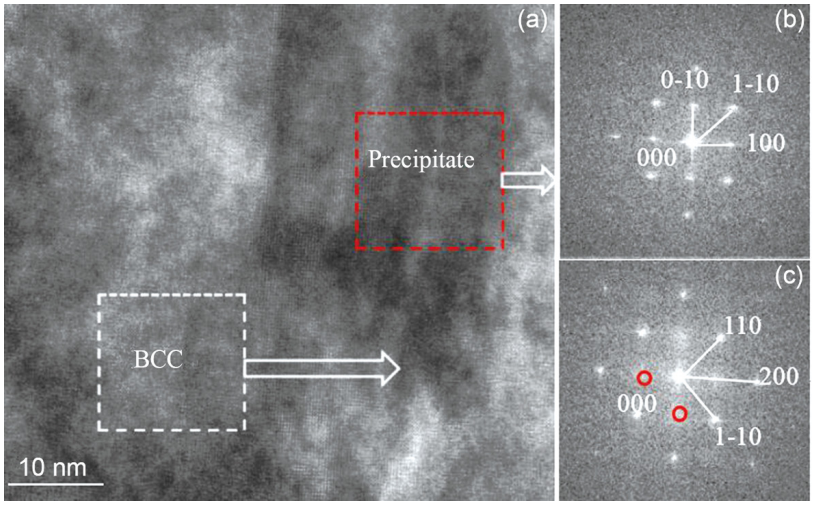

Fig. 7: HRTEM image and FFT map of $AlCrCuFeMn_1$ high-entropy alloy: (a) HRTEM image taken from the <001> direction; (b) FFT pattern of B2 particles; (c) FFT pattern of BCC phase matrix

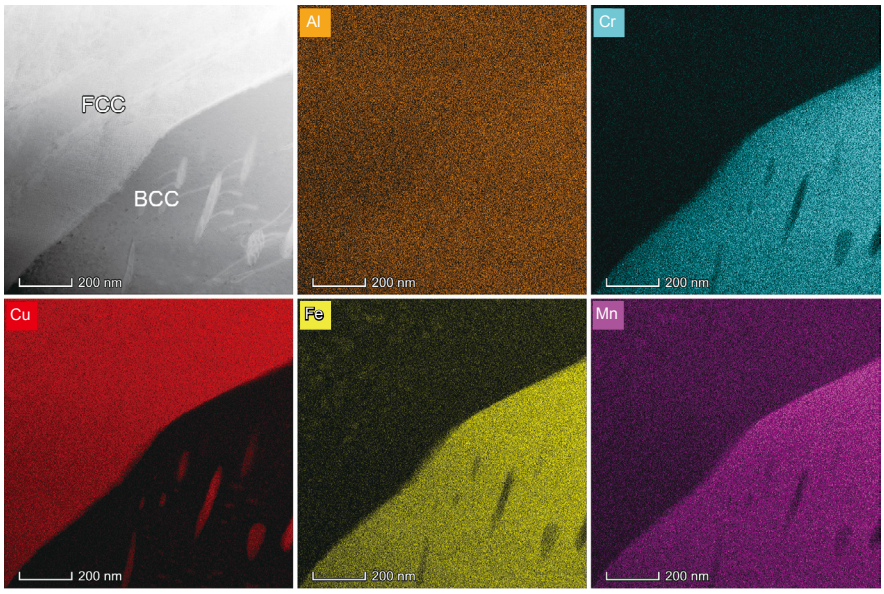

Fig. 8: Element distribution of $AlCrCuFeMn_1$ high-entropy alloy under HADDF and STEM modes

Table 3: Chemical compositions of different phases in AlCrCuFe, AlCrCuFeMn$_1$, and AlCrCuFeMn$_{1.5}$ high-entropy alloys

Alloy	Crystalline	Al	Cr	Cu	Fe	Mn
AlCrCuFe	FCC	10.89	4.59	80.73	3.79	0
	BCC	10.38	42.73	5.85	42.04	0
	Precipitated phase	10.29	22.46	42.48	24.77	0
AlCrCuFeMn$_1$	FCC	16.85	1.31	66.58	2.35	12.91
	BCC	16.70	26.60	2.41	28.62	15.14
	Precipitated phase	21.82	12.50	42.32	14.19	25.67
AlCrCuFeMn$_{1.5}$	FCC	18.89	1.54	57.82	3.14	18.62
	BCC	18.59	38.32	2.35	15.28	25.46
	Precipitated phase	16.91	31.48	19.76	11.71	20.12

The average particle size and area fraction of the precipitated phases on the BCC matrix in the AlCrCuFeMn$_x$ high-entropy alloys were counted using the Image-pro plus software. The results are shown in Table 4. It can be seen that when the Mn content increases, the size of the particles in the precipitated phase firstly increases and then decreases, while the area fraction firstly decreases and then increases. When the Mn content is x=1, the average particle size of the precipitated phase in the dendrites of the high-entropy alloy is the largest.

3.3 Mechanical properties of AlCrCuFeMn$_x$ high-entropy alloys

3.3.1 Compressive properties

Figure 9(a) shows the engineering compressive stress-strain curves of AlCrCuFeMn$_x$ (x=0, 0.5, 1, 1.5, and 2) high-entropy alloys at room temperature, and Fig. 9(b) indicates their yield strength and compressive strength. The AlCrCuFeMn$_x$ (x=0, 0.5, 1, 1.5, and 2) high-entropy alloys are abbreviated as Mn0, Mn0.5, Mn1, Mn1.5, and Mn2, respectively in the following figures and tables. It can be seen from Fig. 9 that when no Mn elements are added, the AlCrCuFe alloy exhibits the highest yield strength of 1,050 MPa, but the lowest compressive strength of 1,125 MPa and deformation rate of 9% compared to the other four alloys. When the Mn element is added, the deformation rate and yield strength change in the opposite direction: the yield strength decreases while the deformation rate increases. As the Mn content is increased to x=1.5, the compressive strength of the alloy reaches its peak value of 1,700 MPa, which is the highest among all experimental alloys. Moreover, the yield strength of the alloy is 960 MPa, and the deformation rate is 27.5%. In summary, these findings suggest an overall optimal performance of the AlCrCuFeMn$_{1.5}$. With further increase of Mn content to x=2, both the yield strength and compressive strength of the alloy decrease, while the deformation rate slightly increases.

The yield strength of the AlCrCuFeMn$_x$ high-entropy alloys is primarily determined by its dendritic structure, which constitutes the majority of the alloy's microstructure. The yield strength

Table 4: Particle size and area fraction of precipitates with different Mn contents

Alloys	Mn0	Mn0.5	Mn1	Mn1.5	Mn2
Particle size (nm)	110	123	169	132	120
Area fraction (%)	20.2	15.1	19.8	22.9	23.1

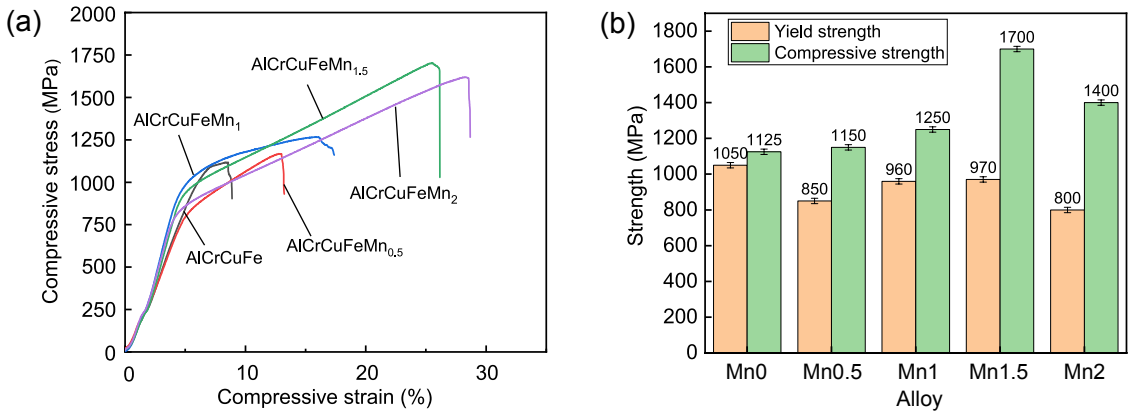

Fig. 9: Stress-strain curve (a) and statistical graph of yield strength and compressive strength (b) of AlCrCuFeMn$_x$ high-entropy alloys

of the dendritic structure is influenced by various factors, including solid solution, grain boundaries, dislocations, and precipitates [23]. The yield strength of the alloy can be calculated according to Eq. (5):

$$\sigma_{0.2}=\sigma_0+\sigma_P+\sigma_S+\sigma_G+\sigma_D \quad (5)$$

where σ_0 is the intrinsic strength of the alloy, σ_S, σ_G, σ_D, and σ_P represent the strengthening effects caused by the solid solution, grain boundaries, dislocations, and precipitates, respectively. Taking the $AlCrCuFeMn_{0.5}$, $AlCrCuFeMn_1$, and $AlCrCuFeMn_{1.5}$ alloys as examples, the average grain size of these three alloys is almost the same, and the only factor affecting their microstructure is the precipitated phase. In addition, the composition of these three alloys is almost the same (Fig. 2), and they were formed under the same casting conditions. Therefore, the difference in yield strength of the alloy mainly comes from the strengthening effect of the precipitates in the dendrite structure.

The precipitation strengthening can be divided into two types based on the interaction between dislocations and precipitating particles: particle shearing and Orowan bypassing mechanisms [24]. The shear mechanism dominates when the precipitated particles are small or have a co-grid relationship with the matrix, while the bypass mechanism becomes dominant when the precipitated particles have a large size or do not co-grid with the matrix [25, 26]. Based on the morphology of the precipitates on the BCC matrix of the $AlCrCuFeMn_x$ high-entropy alloys, it can be determined that the particle shearing mechanism plays a major role in the strengthening.

When calculating the strengthening effect of the shear generated by precipitates, three factors are taken into account: the lattice dispersion strengthening ($\Delta\sigma_{cs}$), modulus mismatch strengthening ($\Delta\sigma_{ms}$), and ordering strengthening ($\Delta\sigma_{os}$). The first two factors contribute prior to the shear, while the latter factor contributes during shear. The expressions of $\Delta\sigma_{cs}$, $\Delta\sigma_{ms}$, and $\Delta\sigma_{os}$ are given in Eqs. (6), (7), and (8), respectively [27, 28]:

$$\Delta\sigma_{cs}=M\cdot\beta_\varepsilon(G\cdot\varepsilon)^{3/2}\left(\frac{rf}{0.5G\boldsymbol{b}}\right)^{1/2} \quad (6)$$

$$\Delta\sigma_{ms}=M\cdot 0.0055(\Delta G)^{3/2}\left(\frac{2f}{G}\right)^{1/2}\left(\frac{r}{\boldsymbol{b}}\right)^{\frac{3m}{2}-1} \quad (7)$$

$$\Delta\sigma_{os}=M\cdot 0.81\frac{\gamma_{APB}}{2\boldsymbol{b}}\left(\frac{3\pi f}{8}\right)^{1/2} \quad (8)$$

where M=2.73 (for BCC) is Taylor Factor, β_ε=2.6 is a constant, G=83 GPa is shear modulus of the matrix, ε=0.2% is the lattice misfit. $\boldsymbol{b}$ is Burgers vector, which can be calculated by $\boldsymbol{b}=\sqrt{3}\alpha/2$, where α is the lattice parameter of the matrix. r is the average diameter of precipitates, f is volume fraction of precipitates, ΔG=83–80=3 GPa is shear modulus difference between the matrix and precipitates [29], m=0.85 is a constant, and γ_{APB} is the antiphase boundary (APB) energy.

In principle, the highest values of $\Delta\sigma_{cs}+\Delta\sigma_{ms}$ and $\Delta\sigma_{os}$ determine their outcome of the contribution [30]. Table 5 presents the values for dispersion strengthening, modulus mismatch strengthening and ordered strengthening due to the addition of Mn elements, calculated from Eqs. (6)–(8). The calculation results show that the sum of $\Delta\sigma_{cs}+\Delta\sigma_{ms}$ is far greater than $\Delta\sigma_{os}$ for $AlCrCuFeMn_{0.5}$, $AlCrCuFeMn_1$, and $AlCrCuFeMn_{1.5}$ alloys. Therefore, lattice dispersion strengthening and modulus mismatch strengthening play a major role in the shear mechanism. The $\Delta\sigma_{cs}+\Delta\sigma_{ms}$ of the $AlCrCuFeMn_1$ and $AlCrCuFeMn_{1.5}$ alloys are 851 MPa and 870 MPa, respectively, which are greater than that of the $AlCrCuFeMn_{0.5}$ high-entropy alloy (766 MPa). This indicates that the strengthening effect of the precipitates of the alloy increases with increasing Mn content.

Table 5: Calculation results of $\Delta\sigma_{CS}$, $\Delta\sigma_{MS}$ and $\Delta\sigma_{OS}$ for $AlCrCuFeMn_x$ (x=0.5, 1 and 1.5) high-entropy alloys

Alloy	σ_{cs} (MPa)	σ_{ms} (MPa)	$\Delta\sigma_{os}$ (MPa)	$\Delta\sigma_{cs}+\Delta\sigma_{ms}$ (MPa)
$AlCrCuFeMn_{0.5}$	719	47	154	766
$AlCrCuFeMn_1$	797	54	124	851
$AlCrCuFeMn_{1.5}$	819	51	131	870

Combined with the analysis above, in the $AlCrCuFeMn_x$ (x=0, 0.5, 1, 1.5, 2) high-entropy alloys, when the Mn increases, the AlCuMn-rich FCC phase starts to increase and the FeCr-rich BCC phase gradually decreases, which results in a general trend of decreasing yield strength and increasing plasticity. However, when the Mn content increases, the area fraction of the precipitated phase in the alloy gradually increases and the size of the precipitated phase is larger in $AlCrCuFeMn_1$ and $AlCrCuFeMn_{1.5}$ compared to $AlCrCuFeMn_{0.5}$ alloy, therefore, when x increases from 0.5 to 1.5, the strengthening effect of the precipitated phase on the alloy is enhanced, resulting in a significant increase in the yield strength of the alloy [31].

3.3.2 Hardness and elastic modulus

Figure 10 shows the microhardness statistics of the $AlCrCuFeMn_x$ high-entropy alloys. The alloy exhibits a hardness of approximately 470 HV when no Mn element is added, which is the highest among the five alloys. However, an increase in Mn content results in an overall decreasing trend in hardness, except when the Mn element content x increases from 1 to 1.5. In this range, the hardness increases. Once the Mn element content exceeds 1.5, the hardness of the alloy decreases again.

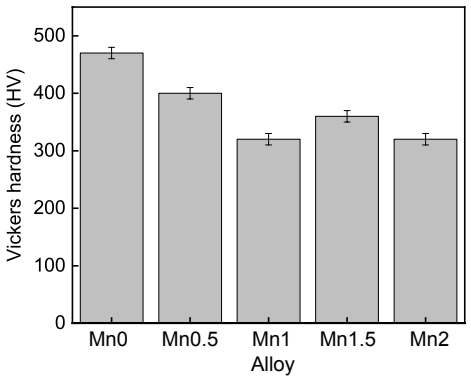

Fig. 10: Microhardness of $AlCrCuFeMn_x$ high-entropy alloys

Figure 11(a) shows typical nanoindentation load-displacement (P-h) curves for the FCC and BCC phases in the AlCrCuFeMn$_x$ high-entropy alloys. The P-h curves show that the maximum indentation depth of the BCC phase is approximately 220 nm, which is much smaller than that of the FCC phase (approximately 430 nm). This indicates that the hardness of BCC phase is higher than that of FCC phase. It is observed that an increase in Mn content initially leads to a decrease in hardness of the BCC phase, followed by an increase, and then another decrease. On the other hand, the hardness of the FCC phase remains almost unaffected when compared to BCC. When no Mn element is added, the nanohardness of BCC phase is the highest (7.26 GPa). While, as the Mn content increases to x=2, the hardness is the lowest (4.78 GPa). Figure 11(c) shows the elastic modulus of different phases. It can be seen that an increase in Mn content initially causes a decrease of elastic modulus for both BCC and FCC phases, followed by an increase, and then another decrease. The FCC phase has approximately 60 GPa lower modulus of elasticity than the BCC phase.

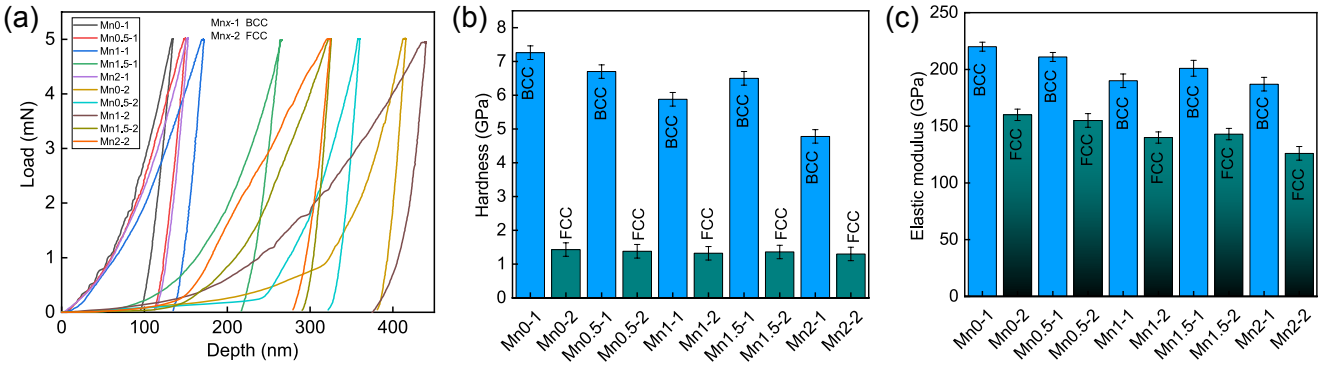

Fig. 11: Loading-displacement curves (a); nanoindentation hardness (b); and elastic modulus (c) of different phases in AlCrCuFeMn$_x$ high-entropy alloys

It can be concluded from the SEM, EDS, and TEM microstructure analysis that the area fraction of BCC phase in the AlCrCuFeMn$_x$ high-entropy alloys gradually decreases while that of FCC phase gradually increases with an increase in Mn content. This causes the hardness and elastic modulus of the alloys to gradually decrease. The size of the precipitates in the dendrites firstly increases and then decreases, as the Mn content increases, while their area fraction firstly decreases and then increases, as shown in Table 4. In the as-solidified condition, strengthening by the precipitates can be described using the rule of mixtures [32,33]:

$$HV_{alloy}=V_{BCC}HV_{BCC}+V_{FCC}HV_{FCC}+V_{P}HV_{P} \quad (9)$$

where V_{BCC}, V_{FCC} and V_P are respectively the volume fractions of the BCC, FCC solid solution and precipitates, and HV_{BCC}, HV_{FCC} and HV_P are their hardness. The hardness of the precipitates was found to be 500–600 HV by nanoindentation. Therefore, HV_P=550 HV was used in further calculations. It should be noted that the grain boundary strengthening was not taken into account due to extremely large matrix grain size in the studied alloys. The estimated contribution of dislocation hardening was no more than 5 HV and thus also neglected. Effect of different phases on the hardness of the AlCrCuFeMn$_x$ high-entropy alloys was calculated by Eq. (9), and is shown in Fig. 12. Figure 12 shows that the AlCrCuFeMn$_x$ (x=0, 0.5, 1, 1.5, 2) high-entropy alloy's hardness is primarily contributed by BCC (53% to 74%), followed by precipitates (17% to 35%), and then FCC (6% to 12%). As the Mn content increases, the contribution of BCC to the hardness of the alloy decreases and that of the precipitates firstly decreases and then increases. When the Mn

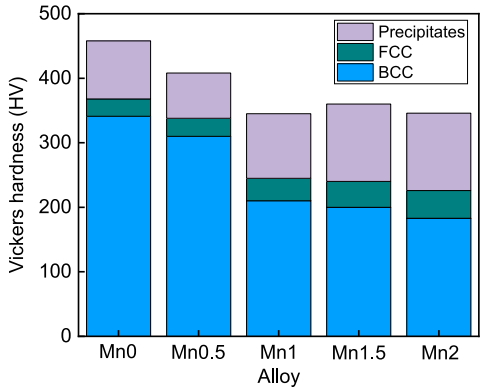

Fig. 12: Predicted values of microhardness of the AlCrCuFeMn$_x$ high-entropy alloys

element content is x=1.5, the contribution of BCC to alloy hardness is slightly reduced to 56%, while that of the precipitates is enhanced to 33%. This is the reason for the increased hardness and elastic modulus of the AlCrCuFeMn$_{1.5}$ high-entropy alloy compared to the AlCrCuFeMn high-entropy alloy.

When comparing the yield strength and hardness of AlCrCuFeMn$_x$ high-entropy alloys to the Cantor alloy (CoCrFeMnNi)$_{100-x}$B$_x$ [34], it is observed that the yield strengths of both CoCrFeMnNi and (CoCrFeMnNi)$_{100-x}$B$_x$ are lower than that of the AlCrCuFeMn$_x$ high-entropy alloys (Table 6). After 16at.% B is added into the CoCrFeMnNi, the hardness of (CoCrFeMnNi)$_{84}$B$_{16}$ reaches a maximum, slightly exceeding that of AlCrCuFe high-entropy alloy. The cost per kilogram of the alloys was calculated based on the price per kilogram of the individual materials in 2022. Next, the cost effectiveness of the alloy was determined by dividing the yield strength of

the alloy by its cost per kilogram. The results are shown in Table 6. It can be seen that the AlCrCuFeMn$_x$ high-entropy alloys boast not only superior strength compared to the $(CoCrFeMnNi)_{84}B_{16}$ alloy, but also a lower cost, resulting in a high cost-performance ratio. Therefore, the AlCrCuFeMn$_x$ high-entropy alloys not only exhibit excellent mechanical properties, but also reduce production costs.

Table 6: Performance ratio of AlCrCuFeMn$_x$ alloys and $(CoCrFeMnNi)_{100-x}B_x$ alloy

Alloy	Yield strength (MPa)	Hardness (HV)	Price (CNY per kg)	Cost performance
AlCrCuFe	1,080	470	176.6	6.1
AlCrCuFeMn$_{0.5}$	810	410	173.6	4.6
AlCrCuFeMn$_1$	950	320	170.6	5.6
AlCrCuFeMn$_{1.5}$	960	360	169.2	5.7
AlCrCuFeMn$_2$	790	310	167.4	4.7
CoCrFeMnNi [34]	256	191	391.2	0.7
$(CoCrFeMnNi)_{84}B_{16}$ [34]	730	482	360.4	2.1

3.3.3 Wear resistance

Figure 13 shows the friction coefficient of the AlCrCuFeMn$_x$ high-entropy alloys. It can be seen that the friction coefficient of the AlCrCuFe high-entropy alloy, with Al_2O_3 as the counterpart, ranges between 0.3 and 0.35 when no Mn element is added. As the Mn content is increased in the AlCrCuFeMn$_x$ alloys, the friction coefficient initially decreases, reaching a minimum value of 0.25 when x=1, before increasing again.

Figure 14 shows the wear scar morphology and wear debris morphology of the AlCrCuFeMn$_x$ high-entropy alloys. It can be seen from Figs. 14(a) and (c) that, when x=0 and x=0.5, the worn surface of the alloy is relatively smooth, with only some shallow furrows and a small amount of flake delamination. The wear mechanisms are mainly adhesive wear, abrasive wear, and delamination wear. It can be seen from Figs. 14(b) and (d) that, when x=0 and x=0.5, the alloy has fewer abrasive chips in a dispersed state of small broken particles. This is the reason for the lower coefficient of friction and wear rate of the alloy. The worn surface of the alloy at x=1 and x=1.5 is shown in Figs. 14(e) and (g). It can be seen that there are a large number of flaky layers and the furrows are also significantly deepened. This indicates that the alloy undergoes delamination

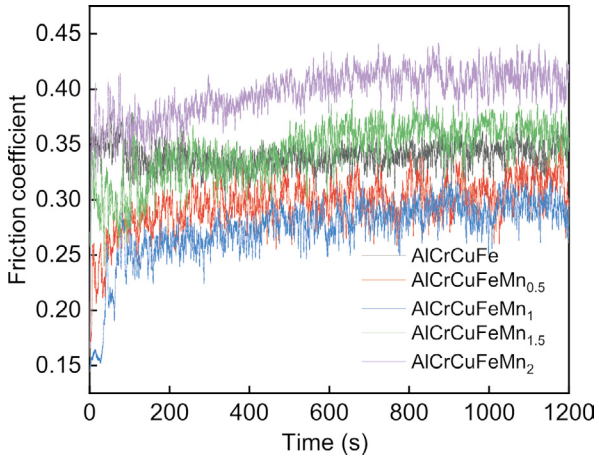

Fig. 13: Friction curves of AlCrCuFeMn$_x$ high-entropy alloys

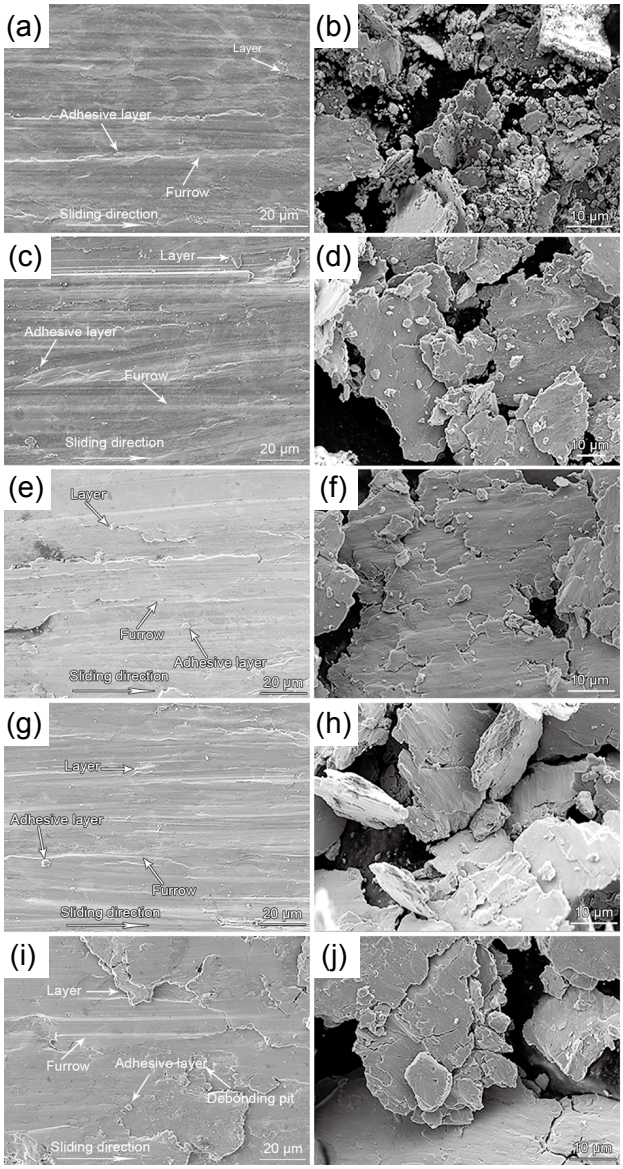

Fig. 14: Wear scar (a, c, e, g, i) and debris (b, d, f, h, j) morphologies of AlCrCuFeMn$_x$ high-entropy alloy: (a), (b) x=0; (c), (d) x=0.5; (e), (f) x=1; (g), (h) x=1.5; (i), (j) x=2

fractures and increased wear. The abrasive chips of the alloy are small piles of particles and flakes, as shown in Figs. 14(f) and (h). When the Mn content x=2, The worn surface of the alloy is shown in Figs. 14(i) and (j). It can be seen that there are adhesion pits and a large number of flaky layers, and the furrows are also significantly deepened. The abrasive chips were in the form of large torn flakes, which are lapped and piled up, and the thickness of the chips also increases, as shown in Fig. 14(j), indicating that more serious wear of the alloy occurs at this composition, which is the main reason for the increased coefficient of friction.

Figure 15 shows the variation of the wear rate of the $AlCrCuFeMn_x$ high-entropy alloys with the Mn content. It can be seen that the wear rate of the alloy is the lowest at x=0. As x increases, the wear rate of the alloy gradually increases, but at x=1.5, it decreases again, and then continues to increase, reaching a maximum value of 2.88×10^{-5} $mm^3\cdot N^{-1}\cdot mm^{-1}$ at x=2. According to Ref. [35], $AlCoCrCuFeNi_{0.5}$ high-entropy alloy exhibits the lowest wear rate of 3.76×10^{-5} $mm^3\cdot N^{-1}\cdot mm^{-1}$ among the $AlCoCrCuFeNi_x$ high-entropy alloys under the same friction conditions, which is obviously higher than the 2.88×10^{-5} $mm^3\cdot N^{-1}\cdot mm^{-1}$. Therefore, the studied $AlCrCuFeMn_x$ high-entropy alloys have better frictional properties.

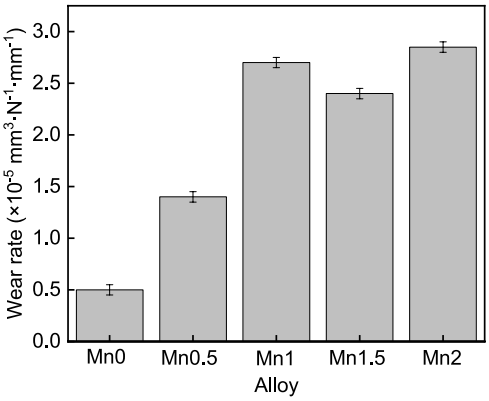

Fig. 15: Wear rate of $AlCrCuFeMn_x$ high-entropy alloys

The variation in wear rate of the $AlCrCuFeMn_x$ high-entropy alloys follows an opposite trend with the variation in hardness. By analyzing the XRD, SEM, and TEM, it can be clearly deduced that as the Mn content increases, the AlCuMn-rich FCC phase increases and the wear resistance of the alloy decreases. However, at the Mn content of x=1.5, the area fraction of the precipitates in the dendrites increases and thus the strengthening effect is enhanced, which leads to an increase in the wear resistance and a decrease in the wear rate of the $AlCrCuFeMn_{1.5}$ high-entropy alloy.

4 Conclusions

(1) The AlCrCuFe high-entropy alloy consists of FCC and BCC phases in its crystal structure, and exhibits a dendritic microscopic morphology. As the Mn element is added, the alloy retains its FCC+BCC phase structure, with an FCC structure in interdendrites, a disordered BCC structure in the dendrites. Additionally, a precipitate phase with an ordered BCC structure forms in the dendrites. With an increase in Mn content, the size of precipitates in dendrites initially increases before decreasing, while their area fraction decreases at first and then increases. Additionally, the addition of Mn elements inhibits the segregation of Cu elements on the FCC phase.

(2) In the $AlCrCuFeMn_x$ (x=0, 0.5, 1, 1.5, and 2) high-entropy alloys, an increase in Mn content leads to a gradual increase in the area fraction of the interdendritic structure of the FCC structure. This results in a gradual increase in plasticity, and a gradual decrease in yield strength, hardness, and modulus of elasticity. However, when x=1.5, the yield strength, hardness, and modulus of elasticity increase again. This is mainly because the increase in area fraction and size of precipitates within dendrites leads to enhanced precipitation strengthening.

(3) The wear mechanisms for the $AlCrCuFeMn_x$ (x=0, 0.5, 1, 1.5, and 2) high-entropy alloys are adhesive wear, abrasive wear, and delamination wear. When no Mn elements are added, the alloy has the lowest wear rate of 0.5×10^{-5} $mm^3\cdot N^{-1}\cdot mm^{-1}$. As the amount of Mn in the alloy increases, both its strength and hardness decrease. Additionally, flaky layers appear on the worn surface, the furrow deepens, and the wear rate of the alloy gradually increases. However, at an Mn content of x=1.5, the alloy's strength and hardness increase due to the enhanced strengthening effect of the precipitates. This results in a lower wear rate and improved friction properties.

(4) The $AlCrCuFeMn_x$ (x=0, 0.5, 1, 1.5, and 2) high-entropy alloys exhibit higher strength than the $(CoCrFeMnNi)_{84}B_{16}$ alloy while also being more cost-effective, resulting in a higher cost-performance ratio. Compared to the $AlCoCrCuFeNi_{0.5}$ high-entropy alloy, the $AlCrCuFeMn_x$ high-entropy alloys exhibit better friction properties and a lower wear rate.

Acknowledgments

This work was supported by the China Postdoctoral Science Foundation Project (2018M633650XB), Gansu Province Young Doctoral Fund Project (2021QB-043), and the CNNC Operations Management Limited R&D Project (QS4FY-22003224).

Conflict of interest

The authors declare that they have no conflict of interest.

References

[1] Chao C Y, Liu C H. Effects of Mn contents on the microstructure and mechanical properties of the Fe-10Al-xMn-1.0C alloy. Materials Transactions, 2002, 43(10): 2635–2642.
[2] Cantor B, Chang I, Knight P, et al. Microstructural development in equiatomic multicomponent alloys. Materials Science and Engineering: A, 2004, 375(377): 213–218.
[3] Miracle D B, Senkov O N. A critical review of high entropy alloys and related concepts. Acta Materialia, 2017, 122: 448–511.
[4] Bharat G, Stephane G, Deep C, et al. Tensile yield strength of a single bulk $Al_{0.3}$CoCrFeNi high entropy alloy can be tuned from 160 MPa to 1800 MPa. Materialia, 2018, 162: 18–23.

[5] Wang X F, Zhang Y, Qiao Y, et al. Novel microstructure and properties of multicomponent CoCrCuFeNiTi$_x$ alloys. Intermetallics, 2007, 15(3): 357–362.
[6] Li X C, Liang H, Zhao Y Z, et al. Microstructure and wear resistance of AlCrFeNiMo$_{0.5}$Si$_x$ high-entropy alloy coatings prepared by laser cladding. China Foundry, 2022, 19(6): 473–480.
[7] Tong C, Chen M, Chen S, et al. Mechanical performance of the Al$_x$CoCrCuFeNi high-entropy alloy system with multiprincipal elements. Metallurgical and Materials Transactions: A, 2005, 36(5): 1263–1271.
[8] Fu Z Q, Chen W P, Fang S C, et al. Alloying behavior and deformation twinning in a CoNiFeCrAl$_{0.6}$Ti$_{0.4}$ high entropy alloy processed by spark plasma sintering. Journal of Alloys and Compounds, 2013, 553: 316–323.
[9] Hsu C Y, Yeh J W, Chen S K, et al. Wear resistance and high-temperature compression strength of FCC CuCoNiCrAl$_{0.5}$Fe alloy with boron addition. Metallurgical and Materials Transactions: A, 2004, 35(5): 1465–1469.
[10] Xing X W, Hu J K, Liu Y, et al. Effect of Mo on microstructure, mechanical and corrosion properties of FeCrNiMnMo$_x$ high-entropy alloys. China Foundry, 2022, 19(6): 464–472.
[11] Hsu Y J, Chiang W C, Wu J K, et al. Corrosion behavior of FeCoNiCrCu$_x$ high-entropy alloys in 3.5% sodium chloride solution. Materials Chemistry and Physics, 2005, 92(1): 112–117.
[12] Michael H, Volodymyr A Y, Marcello B, et al. Materials for hydrogen-based energy storage – Past, recent progress and future outlook. Journal of Alloys and Compounds, 2020, 827: 153548.
[13] Liu Y Y, Chen Z, Shi J C, et al. The effect of Al content on microstructures and comprehensive properties in Al$_x$CoCrCuFeNi high entropy alloys. Vacuum, 2018, 161: 143–149.
[14] Liu S F, Wu Y, Wang H T, et al. Stacking fault energy of face-centered-cubic high entropy alloys. Intermetallics, 2018, 93: 269–273.
[15] Li Z M and Dierk R. Influence of compositional inhomogeneity on mechanical behavior of an interstitial dual-phase high-entropy alloy. Materials Chemistry and Physics, 2018, 210: 29–36.
[16] Dong Z H, Huang S, Valter S, et al. Mn$_x$Cr$_{0.3}$Fe$_{0.5}$Co$_{0.2}$Ni$_{0.5}$Al$_{0.3}$ high entropy alloys for magnetocaloric refrigeration near room temperature. Journal of Materials Science & Technology, 2021, 79: 15–20.
[17] Laplanche G, Berglund S, Reinhart C, et al. Phase stability and kinetics of a sigma-phase precipitation in CrMnFeCoNi high-entropy alloys. Acta Materialia, 2018, 161: 338–351.
[18] Li Z M, Konda G P, Deng Y, et al. Metastable high-entropy dual-phase alloys overcome the strength-ductility trade-off. Nature, 2016, 534(7606): 227–30.
[19] Wu P H, Peng Z, Liu N, et al. The effect of Mn content on the microstructure and properties of CoCrCu$_{0.1}$Fe$_{0.15}$Mo$_{1.5}$Mn$_x$Ni near equiatomic alloys. Materials Transactions, 2016, 57(1): 5–8.
[20] Zhang Y, Zhou Y J, Lin J P, et al. Solid-solution phase formation rules for multi-component alloys. Advanced Engineering Materials, 2008, 10(6): 534–538.
[21] Guo S, N G, Lu J, et al. Effect of valence electron concentration on stability of FCC or BCC phase in high entropy alloys. Journal of Applied Physics, 2011, 109(10): 103505.
[22] Shu D L. Mechanical properties of engineering materials. 2nd Ed. Beijing China: China Machine Press, 2011: 139.
[23] Naoya K, Kensuke S, Goro M, et al. Stress-strain behavior of ferrite and bainite with nano-precipitation in low carbon steels. Acta Materialia, 2016, 83(5): 118–132.
[24] Zhang L J. Study on microstructure and mechanical properties of CrFeNi(CuCo,MnAl) series high entropy alloys. Doctoral Dissertation, Qinhuangdao, Hebei China: Yanshan University, 2019.
[25] Nembach E. Precipitation hardening caused by a difference in shear modulus between particle and matrix. Physica Status Solidi, 1983, 78(2): 571–581.
[26] Argon A S, Bikerman J J. Physics of strength and plasticity. Physics Today, 1971, 24(8): 60–69.
[27] Ardell A J. Precipitation hardening. Metallurgical Transactions: A, 1985, 16(12): 2131–2165.
[28] Gerold V, Haberkorn H. On the critical resolved shear stress of solid solutions containing coherent precipitates. Physica Status Solidi, 1966, 16(2): 675–684.
[29] Zhang G J, Tian Q W, Yin K X, et al. Effect of Fe on microstructure and properties of AlCoCrFe$_x$Ni (x=1.5, 2.5) high entropy alloy coatings prepared by laser cladding. Intermetallics, 2020, 119: 106722.
[30] Morrison C, Dunand D C, Seidman D N, et al. Coarsening resistance at 400 °C of precpitation-strengthened Al-Zr-Sc-Er alloys. Acta Materialia, 2011, 59(18): 7029–7042.
[31] Zeng S, Zhou Y K, Li H, et al. Microstructure and mechanical properties of lightweight Ti$_3$Zr$_{1.5}$NbVAl$_x$ (x=0, 0.25, 0.5 and 0.75) refractory complex concentrated alloys. Journal of Materials Science & Technology, 2022, 130(10): 64–74.
[32] Fakirov S. On the application of the “rule of mixture” to microhardness of complex polymer systems containing a soft component and/or phase. Journal of Materials Science, 2007, 42(4): 1131–1148.
[33] Stepanov N D, Yurchenko N Y, Tikhonovsky M A, et al. Effect of carbon content and annealing on structure and hardness of the CoCrFeNiMn-based high entropy alloys. Journal of Alloys and Compounds, 2016, 687(5): 59–71.
[34] Zhang S J. Effect of B and Y addition on the microstructure and properties of CoCrFeMnNi high-entropy alloy. Master's Dissertation, Harbin China: Harbin Institute of Technology, 2018.
[35] Feng L, Yang W J, Ma K, et al. Microstructure and properties of AlCoCrCuFeNi$_x$ high entropy alloy coating. Chinese Journal of Nonferrous Metals, 1–21 [2022-03-01]. http://kns.cnki.net/kcms/detail/43.1238.TG.20220222.1651.001.html.